STAR HOVERING TEST
- PROOF OF FUNCTIONALITY AND REPRESENTATIVE RESULTS -

F. Hoffmann, O. Schneider, B. G. van der Wall
Institute of Flight Systems, German Aerospace Center (DLR)
Lilienthalplatz 7, 38108 Braunschweig, Germany

R. Keimer, S. Kalow
Institute of Composite Structures and Adaptive Systems, German Aerospace Center (DLR)
Lilienthalplatz 7, 38108 Braunschweig, Germany

A. Bauknecht, B. Ewers
Institute of Aerodynamics and Fluid Mechanics, German Aerospace Center (DLR)
Bunsenstrasse 10, 37073 Göttingen, Germany

K. Pengel, G. Feenstra
German-Dutch Wind Tunnels (DNW)
Voorsterweg 31, 8316 PR Marknesse, The Netherlands

ABSTRACT

Within the DLR project AcTOR (Active Twist Optimized Rotor), a four-bladed, fully instrumented active twist model rotor was built. This active twist rotor was supposed to be tested in the LLF (Low Speed Facility) of DNW within the framework of the international STAR (Smart-Twisting Active Rotor) consortium. The STAR consortium is composed of ONERA, NASA, US Army AFDD, JAXA, Konkuk University, and KARI. In preparation to the planned DNW wind tunnel tests, a comprehensive preparatory test was conducted at the rotor preparation hall of DLR. The aim of this test had been the proof of functionality for the complete wind tunnel model with emphasis on active twist and blade performance. Besides basic rotor data, also advanced data concerning blade deformation and vortex properties for hover applications with and without active twist were aquired. Although, the functionality of the active twist blades and the rotor test stand could be demonstrated successfully, endurance problems occured during the test and hindered the project from a wind tunnel entry. Nevertheless, a comprehensive data base on an active twist model rotor in hover has been gained. The paper provides an overview of the preparatory test and presents representative results.

1. INTRODUCTION

Active rotor control has been subject to intensive research work during the last decades. A lot of different concepts have been investigated theoretically and experimentally, as well as in wind tunnel and flight tests. A survey of the most important research activities is given by Kessler[1,2]. There are two main types of active control used on rotors - blade root and local blade control. In the beginning, mainly concepts applying the control input at the blade root like HHC[3–8] (Higher Harmonic Control) and IBC[9] (Individual Blade Control) have been investigated. Today, research work concentrates on local, blade-integrated control concepts. This includes discrete active trailing edge flaps as well as distributed active twist. Active trailing edge flaps have been successfully tested on a BK117 by Eurocopter[10] and on a MD900 rotor in the Ames wind tunnel by Boeing[11]. Wind tunnel tests with respect to noise and vibration reduction have been carried out by NASA, US Army and MIT in the TDT (Transonic Dynamics Tunnel) at NASA Langley for the ATR[12–16] (Active Twist Rotor).

The principal design of DLR's active twist model rotor blades has been introduced by Riemenschneider et al.[17,18]. The active twist is generated by piezoceramic MFC (Macro Fiber Composite) actuators that are integrated into the upper and lower blade skin. After the investigation of several prototypes in whirl tower tests[19], DLR has now built a four-bladed active twist model rotor as shown in Fig. 1. Since the model rotor was build for wind tunnel testing, it is equipped with numerous sensors. For the measurement of flap-bending and torsion moments 14 strain gages are available whereas 24 strain gages are installed for the application of the SPA (Strain Pattern Analysis) method aiming for the measurement of the blade deformation. Besides, a total number of 186 pressure transducers is distributed within the rotor blades.

Figure 1: Active twist model rotor blades with MFC actuators

The model rotor was intensively tested in hover at the rotor preparation hall of DLR at Braunschweig prior to a planned wind tunnel entry. Basic testing of the rotor included performance analysis like the Figure of Merit and plausibility checks of the measured data, both for the passive and actively controlled rotor. Besides excitations with conventional harmonic controls in the frequency range of 0 to $5/rev$, also individual blade control was applied by means of TPP (Tip Path Plane) splitting with frequencies 0, 1, and $2/rev$. In addition, the actuators were used for the excitation of the blades in order to determine the natural flap and torsion frequencies at different rotational speeds.

In preparation to the wind tunnel tests, advanced measurement techniques were applied at the preparation hall. Accordingly in a first phase of the test, a PIV (Particle Image Velocimetry) and BOS (Background Oriented Schlieren) set-up was installed by DLR in order to carry out measurements of the blade tip vortex. PIV results containing vortex trajectories and instantaneous velocity fields are presented in this paper. The analysis of the BOS measurements is underway and therefore not included here.

The elastic blade deformation was acquired using a SPR (Stereo Pattern Recognition) set-up. The SPR measurements took place during the second test phase, because a parallel set-up of PIV/BOS and SPR equipment was not possible due to shortage of space. In parallel to all SPR measurements carried out by DNW, images of the blade tip were taken by a second independent camera system.

During the tests, an excessively increasing number of cracks developed in the piezoceramics of the MFC actuators with increasing operational time, a problem that had not been occured for predecessor active twist blades. These cracks caused two kinds of failures. On the one hand they damaged the actuators due to short circuits that resulted in burned parts of the actuators leaving inactive actuator areas. On the other hand, there were tiny cracks also causing arcs but not being hot enough to cause burns in the actuators. These cracks caused failures that decreased the actuator performance significantly over time. Due to the reliability and endurance issue with the actuators, a wind tunnel entry was not reasonable for the project.

Despite of the actuator problems, this paper will demonstrate the proof of functionality of the active twist concept as used for the investigated model rotor based on the experimental data gained in the scope of the STAR hovering tests.

2. Experimental Test Set-Up

2.1 Model Rotor

The rotor blades are based on a approximately 41% Mach-scaled design of the Bo 105 rotor blade with a radius of $2\ m$ and a chord of $0.121\ m$. In contrast to the Bo 105 rotor, the model rotor is a fully articulated design without a pre-cone and a clockwise sense of rotation. Nominal rotor speed is $1041\ rpm$. The linear pre-twist was designed to be $-8°/R$ starting at the beginning of the airfoil section which is at $0.44\ m$. However, due to manufacturing problems, the blades possess varying pre-twists with a mean value of approximately $-11°/R$.

As visible in Fig. 2, the rotor blades have been manufactured in two halfs which are glued together via an adhesive film. The C-spar is made of cured unidirectional GFRP (Glass Fiber Reinforced Plastic). Together with a closed cell foam, the spar is glued to the blade skin which consists of two GFRP layers. At the nose, weights made of tungsten rods are added in order to balance the blade. Because of the weight of the actuators, another weight made of bronze is installed right behind the C-spar to maintain the center of gravity at the quarter chord line. Sensor, dummy, and actuator cables are positioned behind the bronze weight.

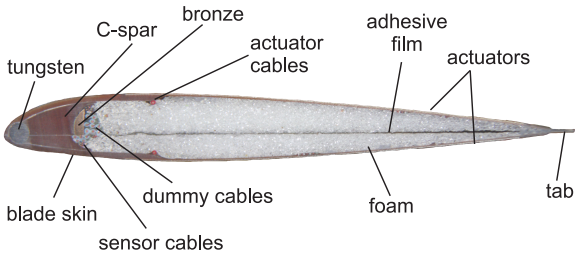

Figure 2: Airfoil cut for blade 3

The active twist is realized by 12 piezoceramic MFC actuators each integrated into the upper and lower blade skin. They are working in a fiber direction of $\pm 45°$ towards the longitudinal blade axis depending on upper and lower side. Always upper and lower actuator patch are grouped as pair and actuated simultaneously. Usually, the actuators are operated at high voltages in the range of $-500\ V$ up to $1500\ V$. Since positive voltages turned out to be critical for the actuators with respect to short-circuits, the maximum voltage was limited to $+600\ V$. In contrast, the min-

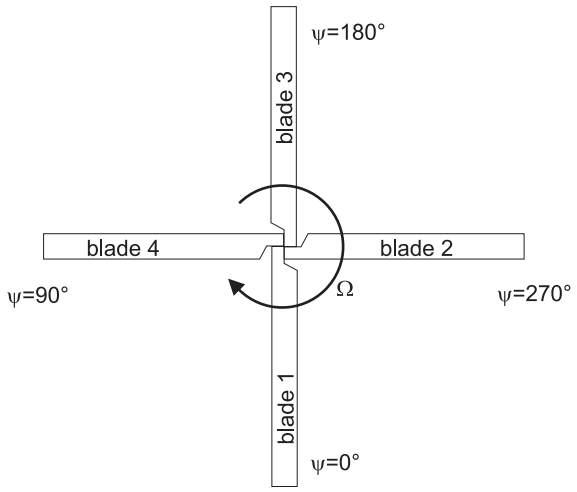

Figure 3: Set-up of the active twist model rotor

imum operational voltage could be extended to $-600\ V$, because no depolarisation effects were observed for this voltage in laboratory. The high-voltage was generated by Trek PZD2000A amplifiers at which three were needed per blade.

The number of sensors differs for the individual blades. Hence, blade 1 and 3 are highly equipped with sensors whereas blade 2 and 4 possess multiple dummy sensors. Also high attention was payed to the compensation of sensor to dummy differences, dissimilarities in the structural blade properties could not completely be avoided refering to Riemenschneider[20]. Thus, a grouping of two similar blade sets turned out such that blade 1 and 3 resemble each other with regard to blade stiffnesses and axis positions as well as blade 2 and 4. As a consequence, similar blades were assembled opposite to each other on the test stand with the blade numbering as given in Fig. 3. Except for the measurement of the fan diagram, where a variation of rotational speed was carried out, all tests were conducted at nominal rotor speed.

2.2 Test Rig

The rotor preparation hall at DLR Braunschweig is a closed atmospheric pressure room with a basement area of $12\ m\ \times\ 12\ m$ and a height of $8\ m$. Here, the model rotor was mounted on the rotor test rig ROTEST II[21] which consists of three major components: a six-component rotor balance carrying all rotor loads, the swash plate actuation system, and the main rotor drive system (a $160\ kW$ hydraulic motor). Blade angles were measured via potentiometers installed at the lead-lag and flap hinge as well as at the hull of the blade attachment for pitch, all at a position of $0.0375R$. Besides the conventional slip ring for the transmission of all sensor signals and their power supply between rotating and non-rotating system, an extra high-voltage slip ring had been installed for the transmission of the high-voltage control signals of the MFC actuators into the rotating system.

The recording of all rotor data was carried out employing a Transputer-based TEDAS II computer with a sampling rate of $1024/rev$, ca. $17.8\ kHz$, triggered by a $1/rev$ rectangular signal. The $1/rev$ signal is the reference signal of the test rig and generated by an azimuth encoder that is connected to the shaft via a tooth belt.

The rotor hub was centered and placed at a height of about $2.76\ m$ without inclination to any side. Therefore, the rotor operated in some ground effect ($z/R\ \approx\ 1.5$, reducing power required) and simultaneously in recirculation (increasing power required). Since the unsteadiness of the flow is increasing with thrust and with it the dynamics of the rotor a compromise regarding the nominal thrust had to be found for the majority of testing. The reference thrust value anticipated for the STAR test in the wind tunnel was defined as $T = 3581\ N$, but for the tests at the preparation hall this had to be reduced to $T\ =\ 2450\ N$. At this thrust level, vibrations and dynamics were small enough to allow for meaningful analysis of the rotor blade motion to pitch control inputs and to active twist inputs. At higher thrust level the vibration and dynamics would have been increased and significantly biased and hindered this analysis.

2.3 Actuator Control

The control signal for the actuators was computed by a Matlab/Simulink-code running on a real time dSPACE-system. The compuation of the control signal was triggered by the $1/rev$ signal and was carried out in collective mode which means that each blade experienced the same control law at the same time.

In order to determine the rotating natural frequencies, the actuators were used to excite the blades with a swept-sine signal. The excitation-voltage was $200\ V$ amplitude sweeping a frequency range from $15\ Hz$ up to $250\ Hz$. The sweep-time was $20\ s$, alternating between rising and falling frequencies to avoid discontinuities. Lower and upper actuator were controlled in phase for the excitation of torsion, whereas actuators had to controlled out of phase between upper and lower skin for a flap excitation of the blade. A sufficient excitation of lead-lag bending is not possible with the actuators. Hence the identification of lead-lag frequencies was not possible.

For harmonic excitation of the blade, which was the main subject of the rotor test, the control voltage $U_i(\psi)$ was defined for the ith blade with $i = 1, 2, 3, 4$ and φ_i as the blade

phase, see Eq. 1.

$$U_i(\psi) = U_{n,i}(\psi) \cdot \cos(n\psi - \varphi_i - \varphi_n) \quad \text{with } \varphi_i = (i-1) \cdot 90^\circ \tag{1}$$

where U_n is the voltage amplitude, φ_n the control phase and n the control frequency as a multiple integer of the rotational speed reaching from 0 to 5. The rotor azimuth is denoted by ψ. No voltage offset was applied, resulting in a maximum control amplitude of $U_n = 600\ V$. A positive voltage amplitude resulted in a nose-down moment.

2.4 Blade Deformation Measurements

Two different optical systems were used to measure the blade deformation independently. A SONY XCD-X710CR camera system acquired the deflection of the blade tip and is called LED (Light Emitting Diodes) camera in the following. Two PCO Sensicam cameras measured the blade deformation along the span based on SPR technique.

The LED camera was installed at the azimuth position of 270° at an external rig. The camera was focused on two permanently illuminated LEDs embedded in the blade tip and located at $23.8\ mm$ and $80.4\ mm$ behind the leading edge in chordwise direction. The camera was triggered by the $1/rev$ signal of the rotor, such that images were always taken with the blade positioned in front of the camera. From the images taken, time series of the LED positions were extracted and accordingly the torsion and flap deflection was computed. Since the tip deflection could only be acquired for one blade at a time with this set-up, measurements were only carried out for blade 1. No calibration of the LED camera was carried out prior to the STAR tests. Only a cross-check between the blade angles measured by the LED camera compared to the angles measured by an angle water level was conducted. Both, mechanical and optical system measurements correlated well.

The SPR technique is based on a 3D reconstruction of the location of markers in space based on stereo images as explained by Müller[22]. Therefore, a pair of cameras was mounted in stereo set-up at a crane at the ceiling of the test hall. The blade deformation was measured analogous to the LED measurements at $\psi = 270^\circ$. The set-up for the SPR measurements is shown in Fig. 4, together with the camera installed for the tip deflection measurements.

On the upper surface of each blade, thirteen markers were distributed each along the leading edge as well as the trailing edge. The local pitch angle could then be determined by means of a marker pair consisting of one marker at the leading and the corresponding marker at the trailing edge. In addition, the flap and lead-lag motion could be determined according to Schneider[23]. The model attitude, the blade azimuthal angle as well as the x-, y- and z-position of the model reference point (rotor hub center) were determined by markers installed on the rotor hub fairing.

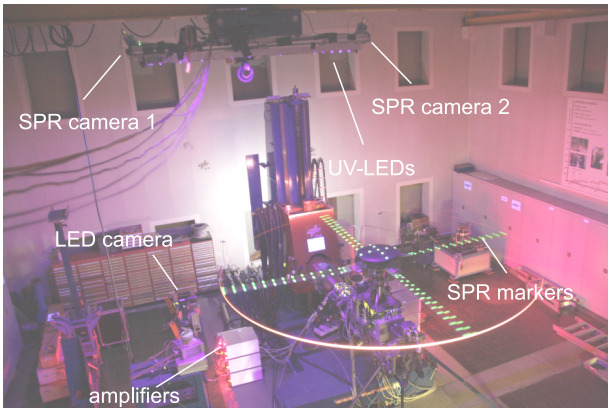

Figure 4: Test set-up for blade deformation measurements

The markers were applied with a fluorescent paint and illuminated by ultra violet light emitting diodes (UV-LED). In order to avoid processing disturbed reflections from the model surfaces, the lenses of the SPR cameras were equipped with single-band bandpass filters (center wavelength = $571\ nm$), so that only the yellow fluorescent markers were visible in the exposures.

For calibration of the SPR system, a calibration board was placed at $\psi = 270^\circ$ and reference images were taken. On the calibration board, numerous balls, also treated with the fluorescing paint, were mounted on different locations with the relative positions of the balls known. Based on these measurements, the transformation matrices, needed for the 3D reconstruction of the marker positions, could be derived.

The SPR cameras had a sensor size of 1374×1040 pixels and a dynamic range of $12\ bit$. The acquisition frequency of the cameras was $4.3\ Hz$. With the rotor speed of $1041\ rpm$ or $17.35\ Hz$, an image was taken by each camera every 4th rotor revolution. The cameras and the illumination of the LEDs were triggered by an impulse sequence derived from the $1/rev$ signal of the rotor. Every 4.25 rotor revolution one impulse triggered the SPR system when a blade was located at $\psi = 270^\circ$. This way, the blades were swept for each image taken. In order to recognize, which blade was exposed, indication markers were installed at the root of the blade, so that the SPR-processing software could recognize each blade automatically.

Both, LED as well as SPR measurements, captured the blade deflection at a certain state of blade motion. To gather a complete cycle of blade motion, it was either necessary to change the position of the camera or to change the phase of the control signal with the camera position fixed in azimuth. Since the latter approach was less time consuming, it was decided to vary the control phase for each data point

in increments of $45°$. This procedure was assumed to be a good compromise between a high resolution of the measurements and the number of configurations that could be tested in the scope of the campaign.

Based on these measurements, a time history representing one period of the blade response with a resolution of eight data points per actuation cycle was composed. Thus, it was technically not feasible to acquire for the entire frequency content of the blade response. For that reason, the blade response was only analyzed for the control frequency content.

2.5 Tip Vortex Measurements

PIV has frequently been applied for phase-averaged flow field investigations on rotating blades over the past two decades, see van der Wall[24] and Heineck[25]. In order to compensate for the aperiodicity of the rotor tip vortices identified from the velocity fields, conditional averaging of the flow velocity field was applied as explained by van der Wall[26]. However, averaged measurements do not show the development of the instantaneous vortices with time, as it can be assessed by high-speed PIV. Hence, the instantaneous flow velocities around the blade tip were determined by means of stereoscopic high-speed PIV as introduced by Raffel[27] during the STAR tests. This measurement technique has been applied for the investigation of the far-field tip vortices of a miniature rotor model in hover by Johnson et al.[28]. In the present measurement campaign, high-speed PIV data was acquired for young tip vortices on a large-scale rotor for the first time. Additionally, density gradient information was simultaneously acquired with a stereoscopic high-speed Background-oriented Schlieren (BOS) system following Raffel[29] . In this paper, a selection of preliminary PIV results is shown. A more detailed evaluation of the flow field data will be given in future publications.

The stereoscopic PIV set-up is illustrated in Fig. 5. It consisted of two PCO Dimax high-speed double frame CMOS cameras, which were equipped with lenses with a focal length of $300\ mm$. The cameras have a sensor size of 2016×2016 pixels and a dynamic range of $12\ bit$. In the current test, the active sensor size was reduced to 1152×820 pixels in order to achieve a high recording frequency of $2.22\ kHz$, which leads to a field of view of $80 \times 90\ mm$ with an azimuthal measurement resolution of $128/rev$ or $2.8°$. Both PIV cameras were rigidly mounted close to the ground beneath the rotor plane and in a Scheimpflug configuration with an angle of approximately $90°$ in between the cameras. To calibrate the PIV system, a two-level calibration target was placed within the field of view of both cameras and at the position of the light sheet prior to each test sequence. Both sides of the target were recorded by the two cameras to determine their relative positions. The height, azimuthal, and radial position of the target are well known by initial measurements and were kept constant throughout the measurement campaign.

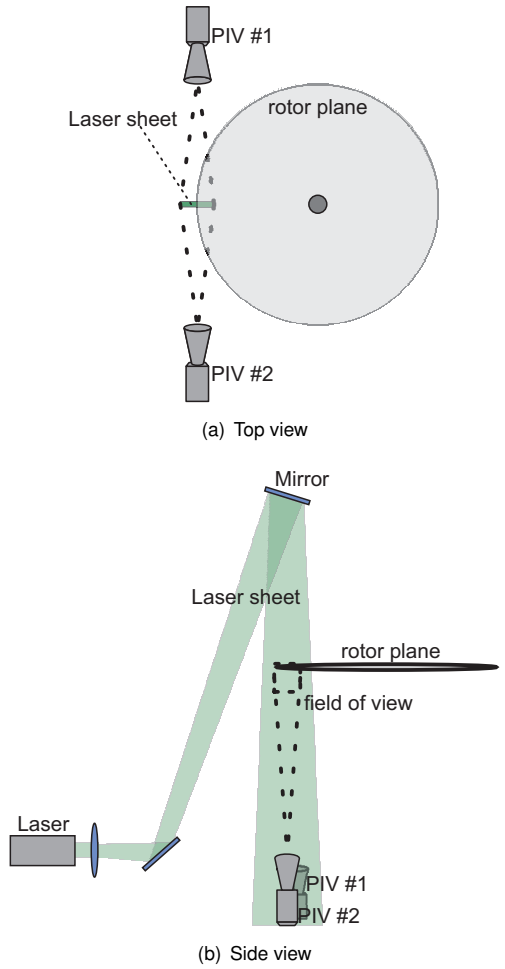

Figure 5: Schematic sketch of the PIV set-up with the two high speed cameras (PIV no. 1 and PIV no. 2), the pulsed laser, and the laser light sheet within the measuring region

An active mode locked Litron LDY 300 Nd:YLF high-speed laser with two separate cavities was used as a light source. The two sequentially generated laser pulses have a temporal length of $5\ ns$ and a pulse energy of $20 - 30\ mJ$, depending on the frequency. A cylindrical lens optic was used to generate a light sheet with a thickness of approximately $2\ mm$ and a length of approximately $300\ mm$ within the measurement region. Using two mirrors mounted behind the optics and above the rotor, the light sheet was projected vertically and with a radial orientation onto the rotor at the $\psi = 180°$ position and close to perpendicular to the tip vortices. The entire rotor testing hall including the measurement region was densely seeded with an aerosol of Di-Ethyl-Hexyl-Sebacate (DEHS) droplets of approximately $1\ \mu m$ diameter. The particle images were recorded and evaluated using the commercial PIV software Davis 8.1.4. A time delay of $30\ \mu s$ was chosen between the

two image acquisitions, corresponding to a blade rotation of $\Delta\psi = 0.2°$. For the evaluation, a multi-grid stereoscopic cross-correlation algorithm with interrogation window sizes between 96×96 and 12×12 pixels with an overlap of 75% was applied. For blade-tip vortex measurements, the ratio of the length of the interrogation window L_m and the vortex core radius r_c has to be as small as possible in order to resolve the vortex dimensions[26]. With the current set-up, core radii of between $r_c = 0.045c$ and $r_c = 0.05c$ were measured, corresponding to a ratio of $L_m/r_c = 0.1$.

3. TEST RESULTS

3.1 Rotor and Test Rig Data

3.1.1 Fan-Diagram

For the analysis of the natural blade frequencies, the FRF (Frequency Response Function) between the excitation signal which was taken from the monitor signals of the amplifiers and the time series of the strain gage signals was computed. Since the identified frequencies vary slightly for the different strain gages depending on their radial position, the mean value of all strain gages (7 each for flap bending and torsion) was taken.

The first flap mode could not be measured since it is a rigid body mode, such that no strains can be acquired by the strain gages due to the lack of elastic bending. However, a good approximation of the first natural flap frequency $\nu_{F,1}$ can be obtained analytically for the hinged rotor according to Eq. 2 with $e_\beta = 0.0375$ as the normalized radial position of the flap hinge.

$$\nu_{F,1} = \sqrt{1 + \frac{3}{2}\, e_\beta} = 1.03 \tag{2}$$

Since the strain gage signals were very noisy for some cases, the identification of the natural blade frequencies was not possible for all measurements. In general, the first two natural torsion frequencies could be determined as well as the natural flap frequencies for the third up to the seventh mode. The resulting fan diagram is shown in Fig. 6 for all blades covering a range of 30 up to 100% nominal rotor speed.

The first natural torsion frequency is crossing the third natural flap frequency at 90% rotor speed causing it slightly to drop to about $3.5/rev$ for blade 1 and 3 and $3.6/rev$ for blade 2 and 4 at nominal speed. The natural frequencies of the third and fourth flap mode correlate very well for all blades with the according frequency at about $4/rev$ and $5.9/rev$ at $100\%\ rpm$. Above the fourth flap mode,

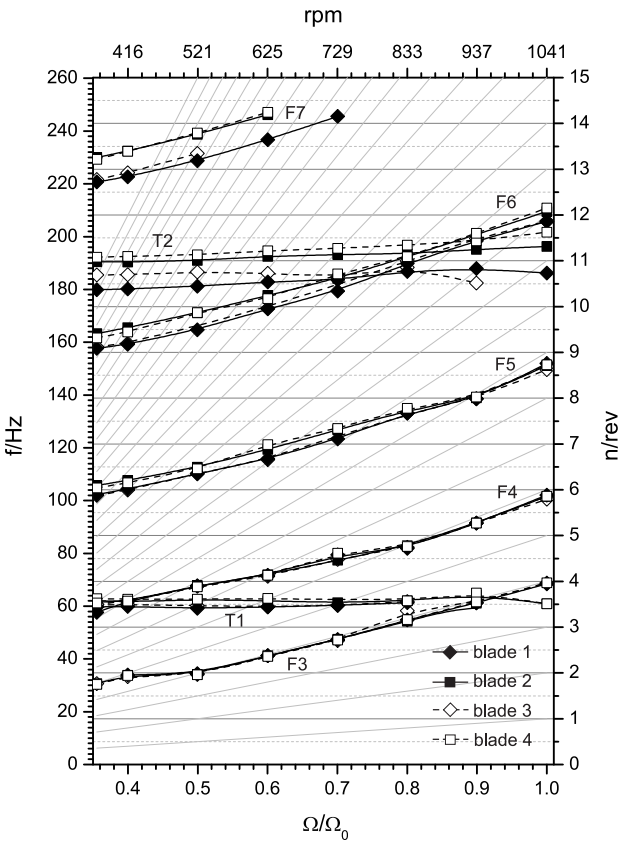

Figure 6: Experimental fan-diagram for the active twist model rotor

a grouping of the results for the two blade sets is developing. The deviating structural properties cause different blade inertias and flap-torsion coupling that become more important with increasing frequency and manifest in different natural frequencies. For the fifth natural flap frequency this grouping is only visible for lower rotational speeds while the flap freqencies match at nominal speed with a value of about $8.7/rev$.

The second natural torsion frequency differs by about $0.3/rev$ between the two blade sets at full rpm. For blade 2 the second natural torsion frequency is detected at $10.7/rev$. This frequency could not be identified for blade 3 but can be assumed to be similar to blade 1 as it was observed for all other frequencies. Analogous, the sixth natural flap frequency for blade 1 and 3 was found at $11.9/rev$ and $12.1/rev$ for blade 2 and 4. For the seventh flap mode, the according natural frequency could not be evaluated for the entire rpm range but the trend is confirmed that for higher frequencies the blade to blade differences in natural frequency are increased.

The natural flap torsion frequencies were identified by a phase-shift of $90°$ and/or a peak in the amplitude of the FRF. While the $90°$ phase shift provides the aerodynamically undamped frequencies, the amplitude peak gives the damped frequencies. In order to estimate the influence of

rpm	amplitude peak		90°-phase shift		$\Delta f_{\vartheta,1}$
	$f_{\vartheta,1}/Hz$	σ_1/Hz	$f_{\vartheta,1}/Hz$	σ_1/Hz	
370	62.47	0.35	61.73	0.37	0.74
416	61.57	0.90	61.75	0.22	-0.18
520	62.62	0.51	62.33	0.39	0.28
625	62.74	0.50	61.80	0.17	0.94
729	61.43	0.32	60.98	0.45	0.45
833	62.30	0.47	61.67	0.06	0.63
936	64.39	0.18	64.05	0.00	0.34
1041	—	—	60.67	0.53	—
rpm	amplitude peak		90°-phase shift		$\Delta f_{\vartheta,2}$
	$f_{\vartheta,2}/Hz$	σ_2/Hz	$f_{\vartheta,2}/Hz$	σ_2/Hz	
370	190.34	0.75	190.53	0.34	-0.19
416	190.24	0.68	190.55	0.22	-0.31
520	190.77	0.60	191.24	0.15	-0.48
625	192.38	0.73	192.62	0.21	-0.24
729	193.05	0.98	193.33	0.47	-0.28
833	193.88	1.14	193.62	0.45	0.26
936	196.17	1.46	194.83	0.37	1.33
1041	195.97	2.17	195.75	0.33	0.22

Table 1: Natural torsion frequencies for blade 2

aerodynamic damping on the natural frequencies detected from the amplitude peak, the variation between un-/damped frequencies was analysed for torsion. Therefore, the natural torsion frequencies $f_{\vartheta,1}$, $f_{\vartheta,2}$ obtained from the 90° phase shift as well as the amplitude peak are given in Tab. 1 for blade 2 together with the standard deviation σ_1, σ_2. Because the amplitude peak is shifted to lower frequency values with increasing aerodynamic damping, the difference between dampend and undamped frequencies should manifest with Δf_ϑ being negative, which is mostly not the case for the first natural torsion frequency as visible from Tab. 1. Taking into account the standard-deviation σ_1 of the measurements, it becomes obvious that differences between damped and undamped frequencies are lower than the uncertainties of the measurement. For the second natural torsion frequency, the difference between damped and undamped frequencies becomes indeed mostly negative, but also lies within the measurement accuracy.

For the natural flap frequencies such a comparison was not possible, since the strain gage signals were to noisy to clearly identify a 90° phase shift. For that reason flap frequencies could only be determined by the amplitude peaks in the FRFs. Although it could be seen that the aerodynamic damping effect is within the measurement accuracy for torsion, higher aerodynamic damping has to be expected for the natural flap frequencies.

3.1.2 Thrust Variation

Rotor performance has been evaluated based on a variation of collective control and thus rotor thrust. In the following,

$\rho,\ kg/m^3$	$a,\ m/s$	C_{d0}	$\Omega,\ rad/s$
1.16	340	0.008	108.3
M_{tip}	κ	$P_0,\ kW$	$C_{l\alpha}$
0.637	1.19	2	6

Table 2: Parameters used for evaluation of the Figure of Merit

measurements for the rotor with and without static active twist are checked for plausibility using momentum theory and the data given in Tab. 2.

The air density ρ was computed from daily measurements of temperature and barometric pressure, while the speed of sound a is derived from temperature only. The air density was measured once a day, but may have varied by daytime. Similarly, the temperature underwent some variations during the day which has an influence on the speed of sound a and thus the Mach number M. This was not taken into account for every individual data point.

The zero drag coefficient C_{d0} is taken from the airfoil polar. Additional empirical values used in the theoretical estimates are the lift curve slope $C_{l\alpha}$ and the induced power factor κ. The average rotational frequency of all data points is represented by Ω with a variation of approximately 0.2% between the data points.

First, the measured collective pitch control required for a given thrust is compared to the collective control estimated by theory refering to Eq. 3.

$$\Theta_0 = \frac{6C_T}{\sigma C_{l\alpha}} + 3\lambda_{eff}\frac{B^2 - A^2}{2} \tag{3}$$

Parameters A and B are the non-dimensional effective radial begin and end positions of the airfoiled section of the blade representing tip losses. The effective inflow ratio λ_{eff} is based on the inflow from momentum theory, multiplied by the induced power factor κ. Since the measured collective is referenced to the representative radius at $0.75R$, the actual amount of linear twist is not part of Eq. 3.

The estimated collective control, measured thrust, and power are plotted in dependence of the measured collective control in Fig. 7. The passive rotor without actuation is represented by the $0\ V$ measurement, whereas for the active rotor a static voltage of $400\ V$ is applied.

In general, the estimated collective agrees well with the measured collective for the passive rotor, but an offset is observed when static active twist is introduced. This is caused by the active twist distribution, which is not relative to the representative radius, rather to the radial begin of actuation at about $0.25R$. Accordingly, the $0.75R$ position has already a lower pitch than the passive rotor, as can be seen in Fig. 7 (a).

Fig. 7 (b) can be discussed in two ways. On the one hand, for the same collective pitch, the change in thrust can be analysed as the vertical distance between passive and active rotor curves at a certain collective pitch. Here, the nose-down twist reduces the rotor thrust by about $280\ N$ due to a smaller angle of attack. In parallel, the total power is reduced as well. On the other hand, for a certain rotor thrust, an additional collective pitch of about 1° is found from the vertical distance between the thrust curves for active and passive rotor. This additional collective pitch is needed to compensate for the nose-down twist generated by the active twist in order to achieve the same rotor thrust and accordingly the same power.

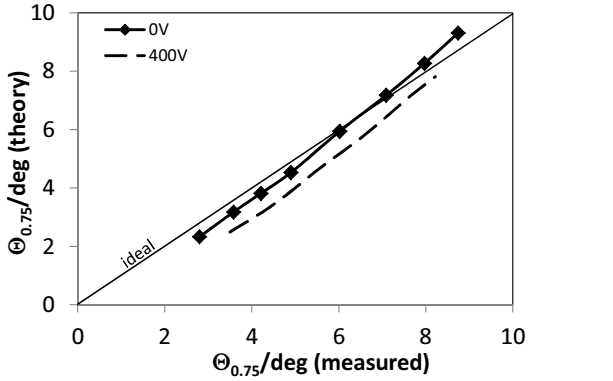

(a) Simulated vs. measured collective

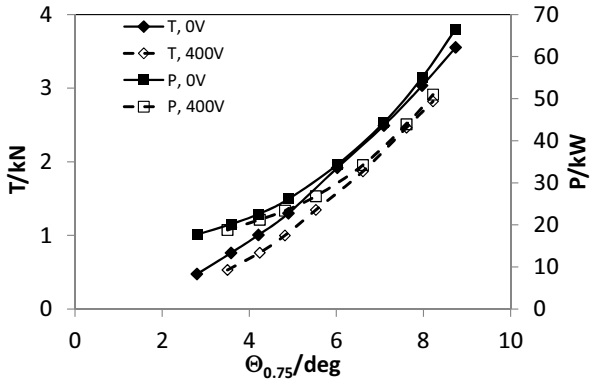

(b) Power and thrust

Figure 7: Collective pitch, thrust, and power of the passive rotor and with active twist actuation

However, from this graph no conclusion can be drawn whether this amount of twist is beneficial for rotor performance or not. This requires the computation of the Figure of Merit FM according to Eq. 4.

$$FM = \frac{P_{ideal}}{P - P_0} = \frac{\sqrt{T^3/(2\rho A)}}{P - P_0} \tag{4}$$

A tare power P_0 measurement without rotor blades attached was performed first, and this tare power was subtracted from the measured power P with blades attached. The ideal power P_{ideal} is based on rotor thrust T only and defined by momentum theory in Eq. 4. The rotor area is denoted by A.

The induced power is based on the induced power factor as given in Tab. 2 as well as a tip loss factor based on Prandtl-Betz as $B = 1 - \sqrt{C_T}/N_b$ with N_b as the number of blades. A comparison of measurement and theory is given in Fig. 8. Although far from maximum thrust of the rotor, the FM curve shows a significant flattening. This indicates that induced power due to recirculation in the closed test hall consumes an increasing amount of extra power, which is not taken into account in the theoretical approach. However, up to $C_T/\sigma = 0.04$ the agreement of theory with experiment is quite well.

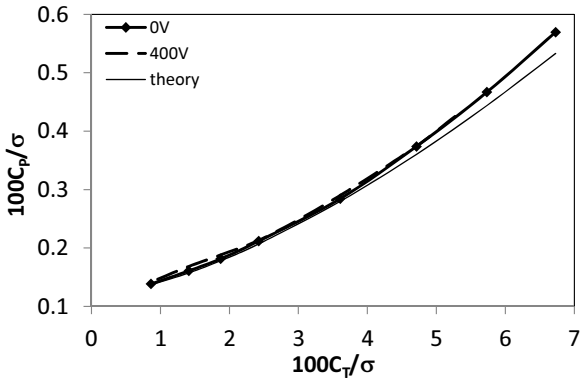

(a) Power

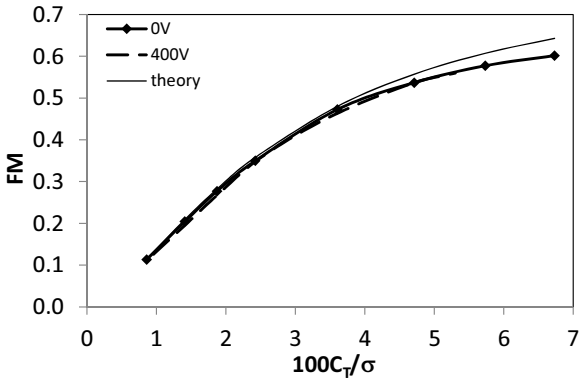

(b) Figure of Merit

Figure 8: Power and Figure of Merit of the passive rotor and with active twist actuation

As can be seen, the actuated rotor has a slight power increase and thus a marginal reduction of FM. This is in contrast to expectations, but within line thickness. The absolute value of power differs between the two curves by less than $0.5\ kW$, which is at the limit of measurement accuracy and may even be caused by a different tare power between the two measurement runs. Numerical studies already indicated that the expected fraction of a degree additional twist will change the power and FM only within line thickness.

3.1.3 Flap and Lag Angles

Flap and lag angles were biased by an unpredictable voltage offset generated by the amplifiers of the data acquisition system as shown in Fig. 9 (a). For zero thrust it is expected that the blades will have almost zero flapping angle and a continuous increase of the mean flapping angle β_0 (positive: flap upwards). Also, the lag angle is expected around zero at no thrust (positive: in rotational direction) and negative values when the thrust is increasing. This is confirmed for all blades in Fig. 9 (a).

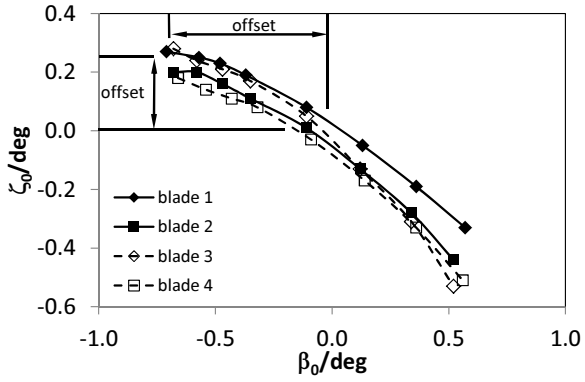

(a) Flap and lag angles

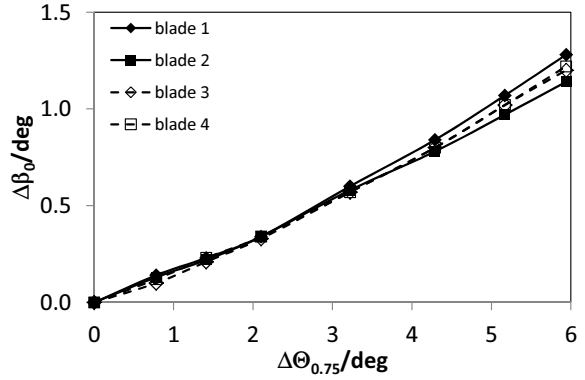

(b) Relative change of flap angles

Figure 9: Flap and lag angle variation with collective control (passive rotor)

Due to the offset problem, only the relative changes can be used for analysis. In general all blades behave quite similar refering to Fig. 9 (b), but it appears that with increasing thrust the blades tend to split in a systematic manner: blade 1 is highest, blade 3 and 4 are about similar and blade 2 is lowest. This is part of the increased vibration when the thrust is increased above the nominal value.

Next, the static flap and lag angles are used to calculate the blade tip position, assuming rigid blades, see Fig. 10. This can be used in comparison with SPR measurements, but it must be understood that with increasing thrust, a different static elastic bending may develop along span which will cause differences between both results. The blade tip flap deflection is reflecting the flap angle as shown before, while the lag deflection causes only about half the deflection for the same increase of thrust, but in a more progressive manner. This follows the behavior of the rotor power. However, the differences between the blades are larger and in a different order than in flapping direction which results from the dissimilarity of the blades.

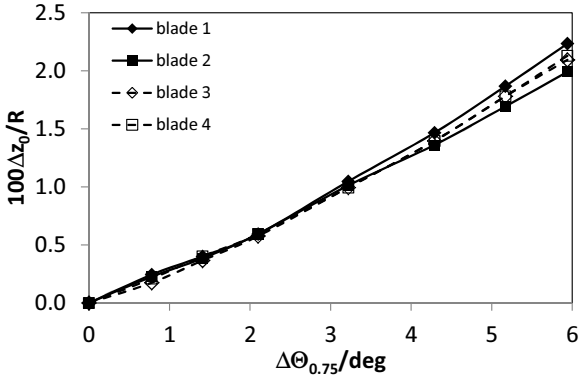

(a) Flap deflection

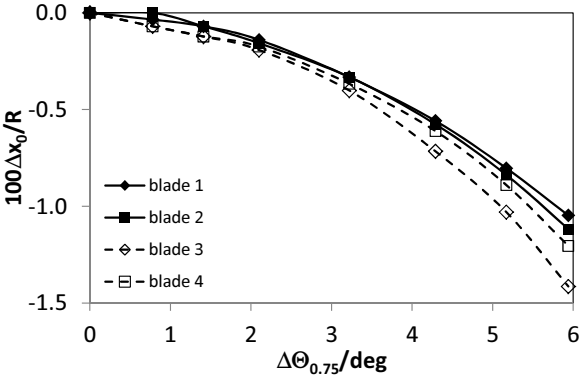

(b) Lag deflection

Figure 10: Relative change of the blade tip deflection (passive rotor)

3.2 Tip Path Plane Splitting

As a new control concept, TPP splitting was tested. TPP splitting is based on a separation of the rotor into two sets of two-bladed rotors in terms of their TPP. The aim of the concept is that tip vortices are released in two different planes such that blade vortex interactions can be assumed to be reduced.

TPP splitting can be performed in three ways. First, the static splitting, where blade 1 and 3 are controlled with a static twist in one direction and blade 2 and 4 in opposite direction. The thrust is unaffected, but the two sets of two-bladed rotors will develop with one having a TPP higher than the other. Second, the $1/rev$ TPP splitting. In this

case, blade 1 and 3 are controlled with a $1/rev$ active twist with a certain phase and blade 2 and 4 experience the same amplitude, but with opposite phase. As a consequence, blade 1 and 3 form a tilted TPP and blade 2 and 4 as well, but their TPP tilts in opposite direction. By proper choice of the phasing, the azimuthal location of maximum separation can be controlled. Third, the $2/rev$ TPP splitting. Here, all four blades get the same $2/rev$ active twist control signal at the same time such they are collectively going up and down with $2/rev$ and the TPP is warped. As an example, blade 1 and 3 may have the maximum position at 0 and $180°$ and are in their lowest position at 90 and $270°$, while blade 3 and 4 have the opposite behavior. The warped TPPs therefore have four locations of maximum separation, and their locations can again be controlled by proper phase of the twist control.

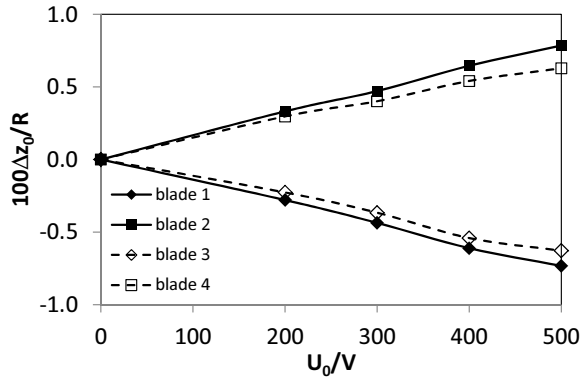

(a) Flap deflection

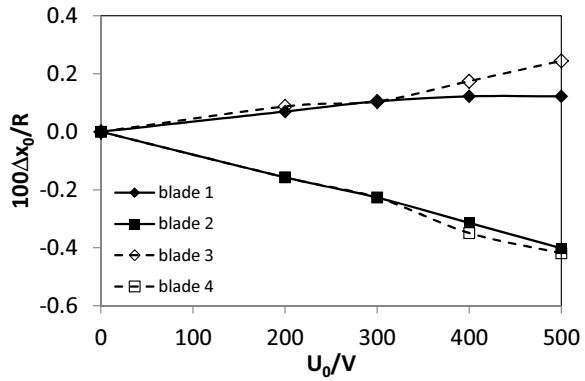

(b) Lag deflection

Figure 11: Relative change of the blade tip deflection ($0/rev$ TPP splitting)

The $0/rev$ TPP splitting result is given in Fig. 11. Blade 1 and 3 are controlled with positive voltage, thus twist down and generate less lift which results in a flap deflection downwards. Blade 2 and 4 experience the opposite sign of voltage, twist up, generate more lift and flap upwards. This behavior is essentially linear in voltage applied. The lag deflection follows the change in lift and consequently in blade drag. Accordingly, blade 1 and 3 move forward in rotational direction due to less lift and thus less drag. Blade 2 and 4 show an opposite response due to increased lift and thus increased drag. Whereas the measured change in flap deflection is in good agreement for all blades, the measured change in lag deflection differs for blade 1 and voltages above $300\ V$. The measured lag deflections change should correlate with the results obtained for blade 3, but probably are biased as a result of lag sensor inaccuracies.

When $1/rev$ TPP splitting is applied, the assumption of rigid blade motion is still justified and blade tip deflections can be computed from flap angles. A reduced variation of control voltages was carried out, since a variation of the control phase was performed in addition. The results are depicted in Fig. 12. For all measurements, the 1/rev blade response of the non-actuated rotor, which was of similar magnitude as the TPP splitting response, has been subtracted. At the highest voltage applied ($500\ V$), blade 1 and 3 obviously have not been controlled at the correct voltage resulting in lower amplitudes than obtained for the other blades. At $300\ V$, the opposite behavior can be observed in Fig. 12 (a).

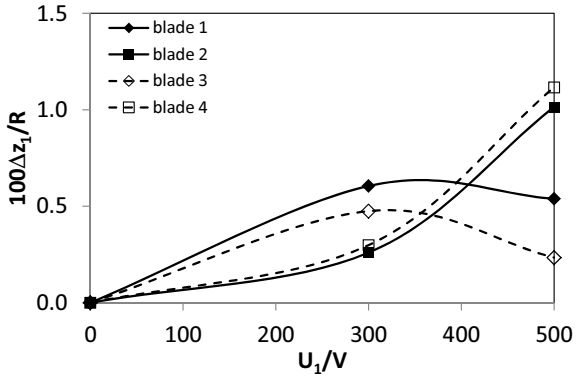

(a) Flap deflection

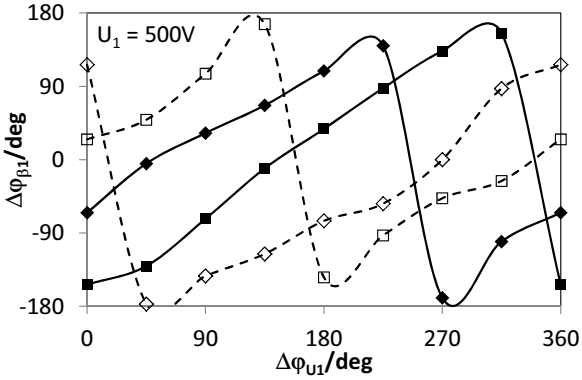

(b) Blade phases

Figure 12: Relative change of the blade tip deflection ($1/rev$ TPP splitting)

In principal, both rotor sets should respond with an identical phase delay to the excitation, but should be seperated by $180°$ due to the TPP splitting. As expected, blade 2 and 4 as well as blade 1 and 3 respond in opposite direction

refering to Fig. 12 (b) whereas deviations from the expected phase of $180°$ result from the 1/rev phase response of the non-actuated rotor which can slightly vary for different measurements. Hence, a complete elimination is not possible and the identified TPP splitting response remains somewhat biased. Relating the phase response between blade 1 and 2, their flap deflections are separated by about $90°$. This means that their individual TPPs are tilted in opposite direction as desired.

Finally, the $2/rev$ TPP is shown in Fig. 13. Analogous to the $1/rev$ TPP splitting results, the $2/rev$ response of the non-actuated rotor has been subtracted. The maximum voltage amplitude applied was $400\ V$, due to excessive vibration. Comparing the amplitudes of deflection for $0/rev$, $1/rev$ and $2/rev$ TPP splitting, the largest deflection is obtained for a $2/rev$ control. However, the actual tip deflection is expected to be smaller due to the proximity of the second flap mode in its natural frequency. Accordingly, significant elastic blade bending can be expected such that rigid blade assumptions might overestimate the tip deflection. Though for consistency of representation, again the blade tip deflection is computed assuming a rigid blade.

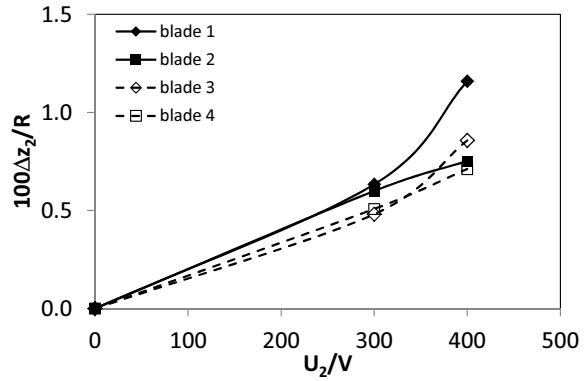

(a) Flap deflection

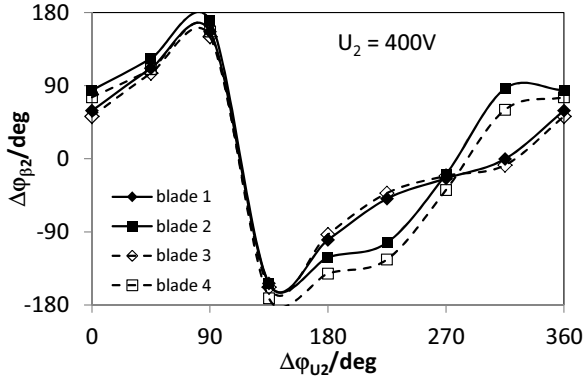

(b) Blade phases

Figure 13: Relative change of the blade tip deflection ($2/rev$ TPP splitting)

From the measured data, a linear increase in deflection amplitude with voltage is indicated and the phase of motion principally is the same for all blades, i.e., they do the same at the same instant of time as desired for this type of control. Blade to blade differences in the phase response result from the $2/rev$ blade motion of the non-actuated rotor which could not be completely eliminated by subtracting. This part of the test demonstrates the feasibility of the TPP splitting concept. Whether this actually is able to reduce BVI noise is left open until the wind tunnel test is performed.

3.3 Blade Deformation

3.3.1 Thrust Variation

Collective pitch as well as torsion and flap tip deflection are illustrated versus thrust in Fig. 14 for the passive and active rotor examplarly for blade 1. Since a positive voltage generates a nose-down moment on the rotor blade, the active twist control is increasing the blade twist. The increase in elastic twist is in the magnitude of $\Delta\vartheta_{tip} \approx -1.1°$. To compensate the additional twist, higher collective of about $\Delta\theta_{0.75} \approx 1°$ is necessary to achieve the same rotor thrust as already observed from Fig. 7. Resulting, the blade tip is less loaded and the flap deflection at the tip is reduced by $\Delta 100 z_{tip}/R \approx 0.2$. In contrast, the static flap angle does not change because passive and active rotor are trimmed to the same thrust.

3.3.2 Static and Harmonic Control

Main subject of the rotor tests was the evaluation of active twist performance for different harmonic controls. Accordingly, the elastic blade response for control frequencies n reaching from 0 to $5/rev$ was measured. Since static control measurements with an amplitude of $400\ V$ were not available, the tip deflection was linearly interpolated from measurements with different static control amplitude. The blade response at the tip as obtained by SPR is plotted for torsion in Fig. 15 and flap bending in Fig. 16. In comparison, the tip deflections measured by the LED camera are plotted for blade 1, correlating well with the SPR results.

Concerning the first natural torsion frequency, which was found at about $3.5/rev$ for all blades, the maximum torsion amplitude can be expected for a $3/rev$ control as it can be seen for blade 2 and 4. Blade 1 and 3 show very similar amplitudes for a 2 and $3/rev$ control, suggesting that the peak in torsion amplitude could be shifted to lower control frequencies compared to blade 2 and 4. In contrast, the LED measurement directly at the blade tip shows the maximum torsion amplitude at $3/rev$ for blade 1 which correlates better with the results for blade 2 and 4. The $90°$ phase shift indicating the passage of the first torsion frequency is crossed between 3 and $4/rev$ in Fig. 15 which is also in accordance

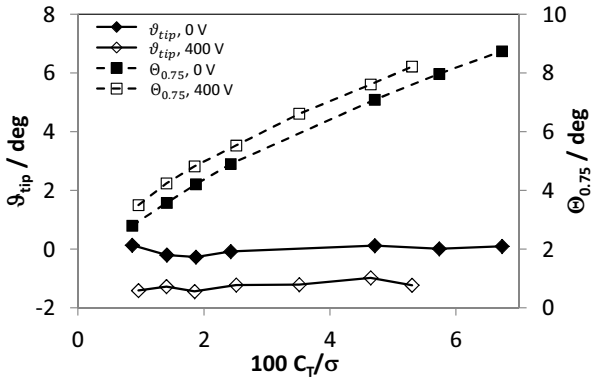

(a) Elastic torsion

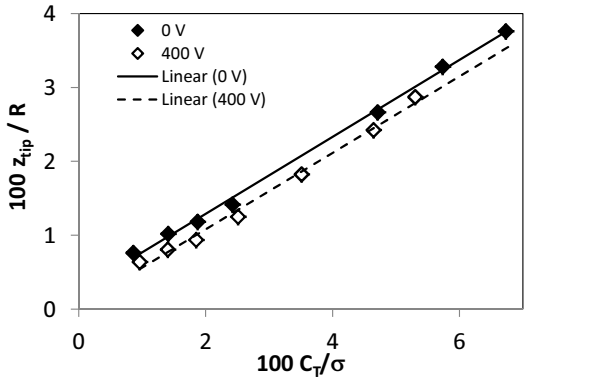

(b) Flap deflection

Figure 14: Blade tip deflection for passive rotor and with active twist actuation

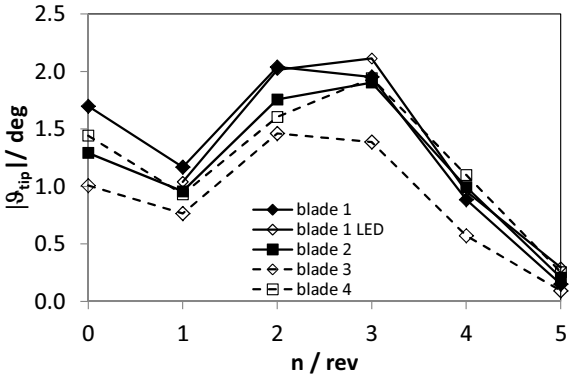

(a) Amplitude

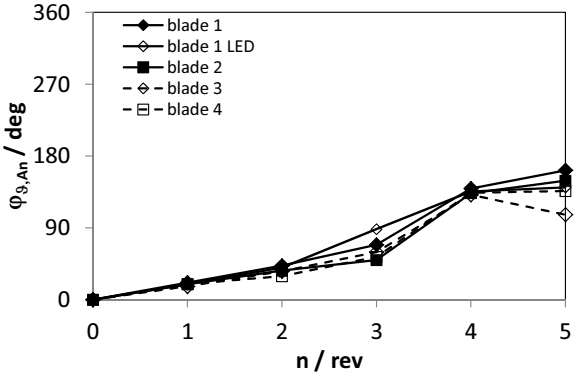

(b) Phase

Figure 15: Elastic torsion at the blade tip for control frequencies n from 0 to $5/rev$, $U_n = 600\ V$

with the torsion frequency idenfied from Fig. 6.

From the grouping of the rotor blades due to their structural differences, a similar blade response would be expected for blade 1 and 3 as well as blade 2 and 4. While good correlation between blade 2 and 4 can be found, the torison amplitude of blade 3 is the lowest and therefore significantly differs compared to blade 1 with the highest torsion amplitude. This deviation probably results from a reduced actuator performance for blade 3 which showed the highest number of cracks in actuator ceramics during the tests.

The $1/rev$ control frequency is very close to the natural frequency of the first flap mode at $1.03/rev$. Resulting, a clear peak in the flap amplitude can be recognized. The phase response can be expected to be dominated by the phase of the first flap mode which should be located slightly below $90°$ for this undercritical excitation. Though, the avarage of the phase delay measured for the different blades was determined at $94°$. Please note, that all phases shown in this paper are corrected for the phase delay included in the control and measurement chain but do not consider phase delays resulting from the acutator hysteresis. This phase delay was found at about $20°$ for an isolated actuator and control frequencies in the range of 1 to $5/rev$. Since this value can be varying for different actuators it is not applicable in general and was not included in the data analysis. Regardless, the measured phase response for flapping can be considered in the right order of magnitude.

A steep decrease in torsion amplitude can be observed for control frequencies above $3/rev$. As the flap motion is only excited by torsion via structural and aerodynamical coupling, the flap amplitude is also strongly reduced. The phase delay in torsion as well as the flap response is increasing with frequency since the blade response is increasingly delayed due to its inertia. The phase response in torsion contains the same phase delay due to the actuator hysteresis as discussed for the flap phase response before.

3.3.3 Modal decomposition of radial deformation

To gain deeper insight into the blade response due to active twist excitation, a modal decomposition of the radial deformation measured by SPR has been carried out for blade 1. Therefore, a least square regression method was employed with the computed mode shapes as the trial function. For comparison, the measured radial deformation is plotted. This measured data can slightly differ from the total

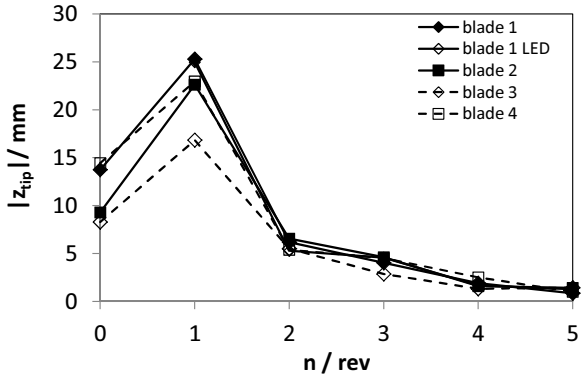

(a) Amplitude

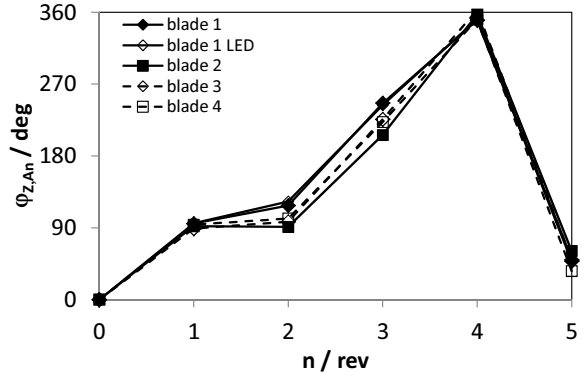

(b) Phase

Figure 16: Flap deflection at the blade tip for control frequencies n from 0 to $5/rev$, $U_n = 600\ V$

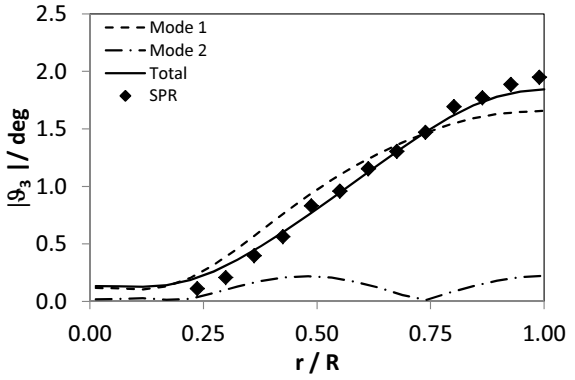

(a) Amplitude

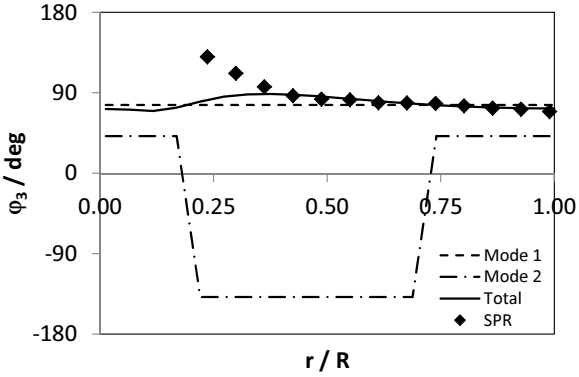

(b) Phase

Figure 17: Modal decomposition of elastic torsion response for $3/rev$ control, blade 1, $U_3 = 600\ V$

blade response computed from the sum of the fitted mode contributions. In the following, the results are exemplary discussed for a selection of control frequencies.

The torsion response to a $3/rev$ control is shown in Fig. 17. The amplitudes and phases versus radius are illustrated for the first and second torsion mode as well as the total torsion amplitude as sum of both mode contributions. For the $3/rev$ control, the first mode shape is clearly dominating the total response, for both amplitude and phase due to the closeness of the control frequency to the first natural torsion frequency. However, the second mode is already contributing with an amount of about 15% to the total amplitude. Since first and second mode shape are both responding in phase to the excitation, they are adding at the blade tip. At the inner part of the blade the second mode is acting out of phase to the excitation because of its node and therefore reducing the total torsion amplitude within the inner blade area.

The influence of the second mode shape is clearly increased for the $5/rev$ control as visible from Fig. 18. Although its magnitude almost remains the same, its contribution to the overall response is increased to 41%. This results from the significantly reduced response of the first torsion mode. In addition, the first torsion mode is now responding out of phase to the excitation, whereas the second mode is nearly acting in phase. Hence, both mode shapes are counteracting at the tip, thus reducing the total torsion amplitude. Consequently, first and second torsion mode are working in phase to each other within the inner blade area, increasing the total torsion amplitude above the blade tip deflection there.

These two examples already show that the radial blade response is highly depending on the excitation frequency. In principal this behaviour also can be observed for flapping. For the $1/rev$ control the blade is mainly responding with its first flap mode due to the closeness of the first natural flap frequency. As explained before, the first flap mode is a rigid body mode as can be recognized from Fig. 19. Higher mode shapes show no meaningful contribution to the total amplitude, except at the blade tip where a small magnitude has been identified for the second mode shape. Its phase should be identified below the phase of the first mode in phase to the excitation. Due to the very small amplitudes computed for these modes, the reliability of the phases computed is strongly decreased.

The response to the $3/rev$ control shown in Fig. 20 is composed of contributions of the first three flap modes whereas the second flap mode is dominating the total deformation

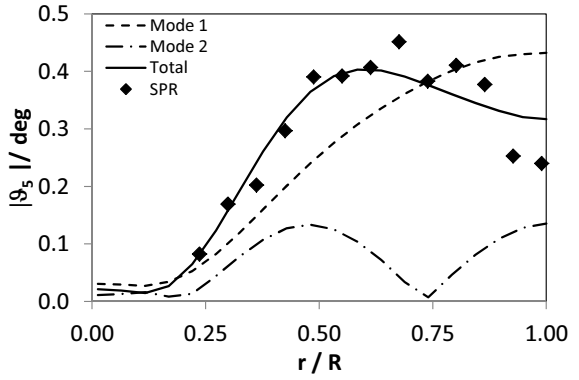

(a) Amplitude

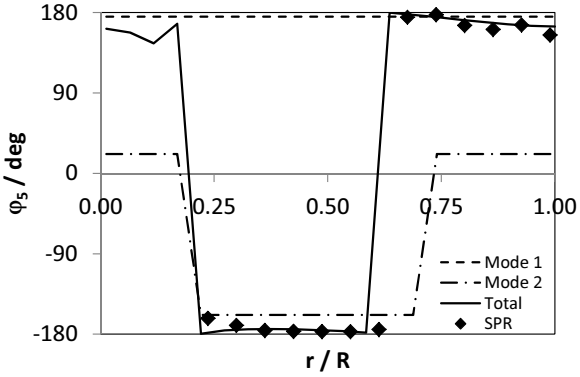

(b) Phase

Figure 18: Modal decomposition of elastic torsion response for $5/rev$ control, blade 1, $U_5 = 600\ V$

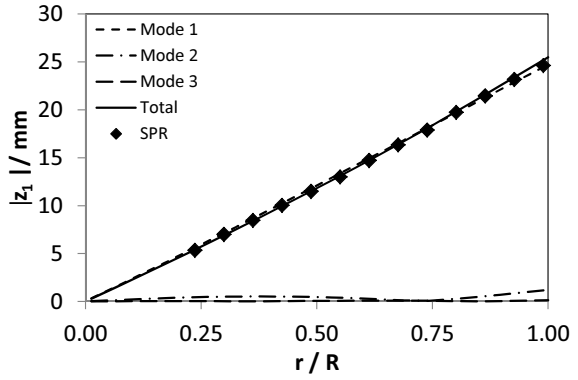

(a) Amplitude

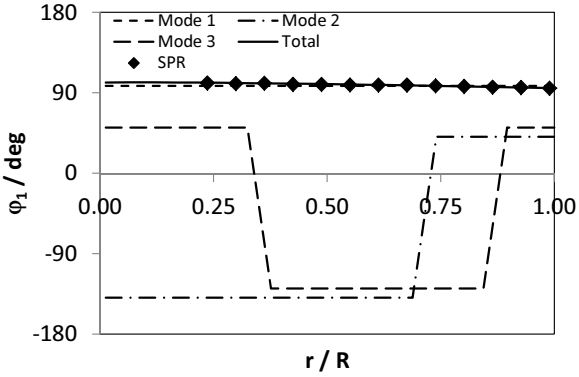

(b) Phase

Figure 19: Modal decomposition of flap response for $1/rev$ control, blade 1, $U_1 = 600\ V$

along radius. First and second mode are working with similar phase in the inner part of the blade. At the blade tip, the 2nd mode is out of phase to the excitation and therefore decreases the total response there. With its natural frequency at about $4/rev$, the 3rd flap mode also contributes with some small amount to the overall deflection.

3.4 Tip Vortex Measurements

3.4.1 Thrust Variation

At first, the influence of rotor thrust on blade tip vortices is studied for the passive rotor. In Fig. 21, the instantaneous velocity fields behind blade 3 at different rotor thrust are depicted. The velocity fields are corresponding to thrust levels of $1330\ N$, $1890\ N$, and $2450\ N$, which correspond to blade loadings of $C_T/\sigma = 0.024$ - 0.044. The rotor mast is located far to the left of the graphs. The blade tip intersects the measurement plane around $x\ =\ 55\ mm$ (horizontal axis), whereas the vertical position depends on the applied rotor thrust. The absolute velocity vectors within the measurement plane are plotted as black arrows and a contour plot of the tangential velocity component v_y is overlaid in the background. All graphs are generated from single PIV images and show the vortices at a vortex age of $\psi_v\ =\ 11.2°$.

The variation of the vertical vortex positions at different thrust levels originate from the increased vertical convection of the wake and the increased blade coning angle with higher rotor thrust. For a rotor thrust of $2450\ N$, the velocity field features a masked region that corresponds to the well-pronounced particle void due to the high centrifugal forces acting on the tracer particles around the vortex core, as described e.g. by Mc Alister[30]. Here, the maximum and minimum tangential velocities on the right-hand side and the left-hand side of the vortex core are of the order of $50\ m/s$ and $-41\ m/s$, respectively. Below and to the left of the tip vortex location, the remains of the shear layer behind the rotor blade and their roll-up into the tip vortex are visible.

In Fig. 22, the tangential velocity component along a horizontal cut through the vortex core and vertically averaged over 20 pixels is depicted. It closely resembles the swirl velocity component around the vortex axis, which has not been evaluated yet. For all three thrust cases, the vortex age was $\psi_v\ =\ 11.2°$. In addition to the measured data, a fitted curve of the Lamb-Oseen vortex model[31] was included for a thrust of $1890\ N$. It can be seen that the measured data features small deviations from the vortex model,

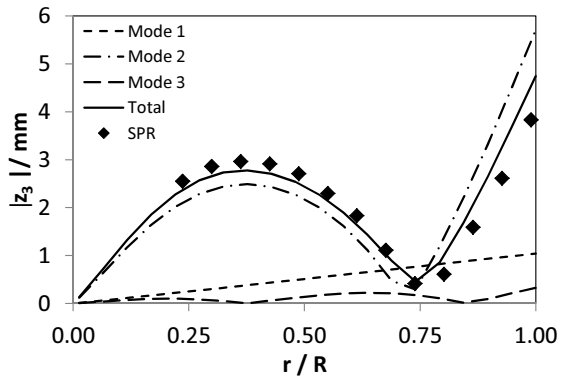

(a) Amplitude

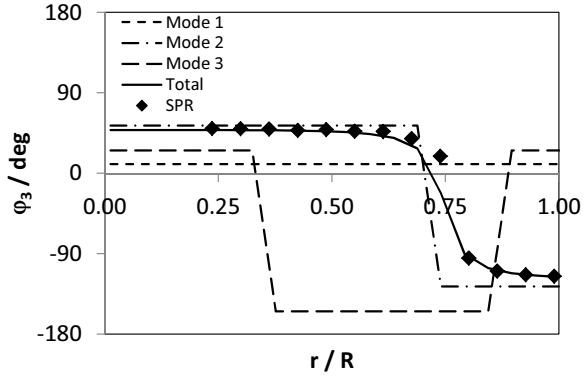

(b) Phase

Figure 20: Modal decomposition of flap response for $3/rev$ control, blade 1, $U_3 = 600\ V$

some of which result from the spatial averaging and the superimposed downwash of the rotor.

In the inset of Fig. 22, the absolute peak-to-peak difference between the maximum and the minimum of the tangential velocity component is plotted as a function of rotor thrust. The magnitude of the vortex-induced velocity field shows proportionality to the rotor thrust and therefore the individual blade loadings.

3.4.2 Harmonic Control

In Fig. 23, the instanteneous velocity fields together with the absolute velocity vectors are given for a $3/rev$ control with an amplitude of $U_3 = 600\ V$ and control phases from $\varphi_3 = 0°$ to $315°$. As explained in Sect. 2.4, the control phase was varied in $45°$ increments in order to capture one period of blade motion in the blade deformation measurements. Since PIV measurements were taken in parallel to the LED measurements, they were also taken for different states of one period of the blade motion.

In principle, the blade is responding to a harmonic excitation as the $3/rev$ control with a harmonic change in elastic

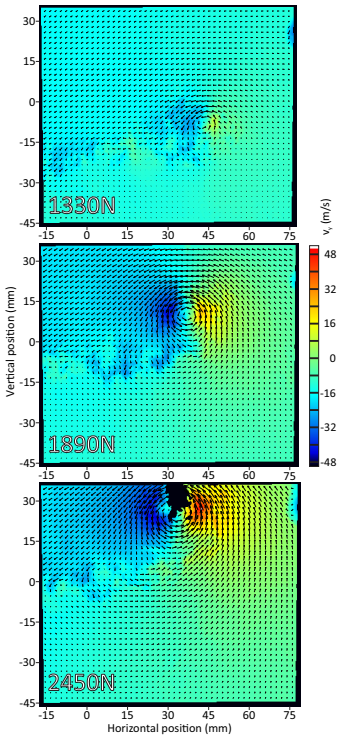

Figure 21: Instantaneous velocity fields around the tip vortex for a thrust variation of the passive rotor, blade 3

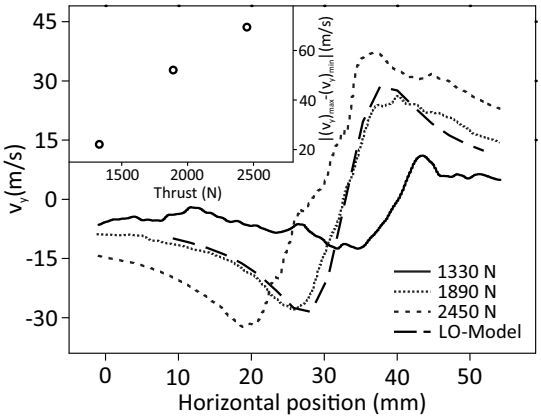

Figure 22: Averaged tangential velocity component around the tip vortex for a thrust variation with the absolute peak to peak difference plotted versus rotor thrust in the inset, blade 3

torsion as well as flap bending at a certain phase delay. Accordingly, the angle of attack is altered harmonically around the baseline condition without actuation. For comparison, the results for the non-actuated case are plotted in the upper left corner of Fig. 23. Since for the $3/rev$ control the modification of the harmonic component of the angle of attack due to unsteady effects is small, the change in angle of attack can be assumed to be directly related to the change in elastic torsion. Resulting, the aerodynamic lift and circulation experience a harmonic change over rotor azimuth causing a harmonic variation in vortex strength.

Because all results are obtained for a vortex age of $\psi_v = 11.2°$, the vortex strength can not be directly related to the blade motion anymore. Nevertheless, it can be seen from Fig. 23 that the instanteneous velocity fields are strongly affected by the active twist control such that the vortex strength and position are changing with control phase. The trajectory of the vortex from its generation up to its instantaneous position is indicated by a red arrow.

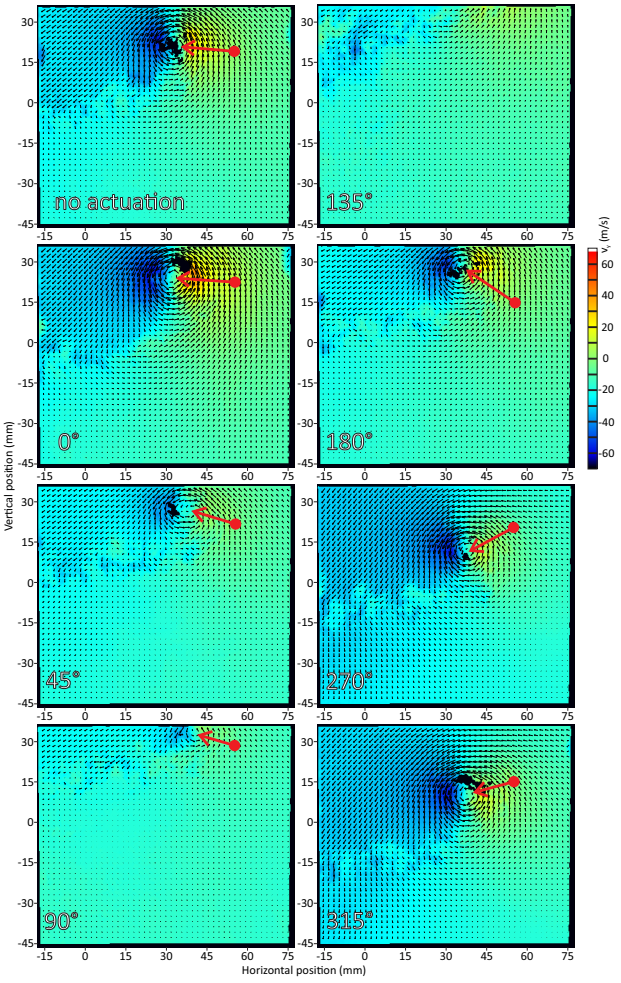

Figure 23: Instantaneous velocity fields around the tip vortex at different control phases of a $3/rev$ control and a vortex age of $\psi_v = 11.2°$, blade 3, $U_3 = 600V$

The influence of the actuation on the vortex strength can be observed in more detail in Fig. 24. Here, the averaged vertical velocity component is plotted along horizontal cuts through the vortex cores for selected control phases. In addition, the peak-to-peak difference between the minimum and maximum tangential velocity is plotted in the inset. The lower/higher the peak-to-peak difference, the lower/higher the vortex strength. The minimum vortex strength should be observed for control phases at which the minimum elastic torsion is achieved right at the azimuth where the PIV image is taken. The phase delay in torsion response was determined at about $70°$ from the LED measurements for blade 3. Accordingly, the minimum torsion amplitude and therefore minimum vortex strength should be achieved for a control phase of approximately $90°$. This is in accordance to Fig. 24, where the minimum difference in tangential velocity was identified at a control phase of $90°$ and $15\ m/s$.

As minimum and maximum peak-to peak-difference should be in the same order of magnitude, the maximum vortex strength would be expected for control phases between $270°$ and $315°$ from the measurements. This correlates to the measured phase delay in torsion. Although, a slight increase of the tangential velocity compared to no actuation is found for $0°$ with a maximum peak-to-peak difference of about $88\ m/s$, the vortex strength equals the values obtained for the passive rotor for control phases of $270°$ and $315°$. This deviation between theory and measurement probably originates for several reasons.

First, LED measurements were not carried out at the same azimuth position as the PIV measurements and therefore can differ from the actual state of blade motion at which the PIV measurement was acquired. Though, the LED measurements should reflect the principal trends of the blade response. In addition, the PIV images were not captured right behind the blade but at an age of $\psi_v = 11.2°$. Hence, the vortex strength could already have been reduced compared to the point of time when it was released from the trailing edge of the blade. However, the main reason for the differences probably result from the data analysis of single PIV images, which means that the instanteneous velocity fields are not averaged and contain all fluctuations evident within the flow field. Accordingly, fluctuations between individual measurements could limit the comparibility of the results for different control phases.

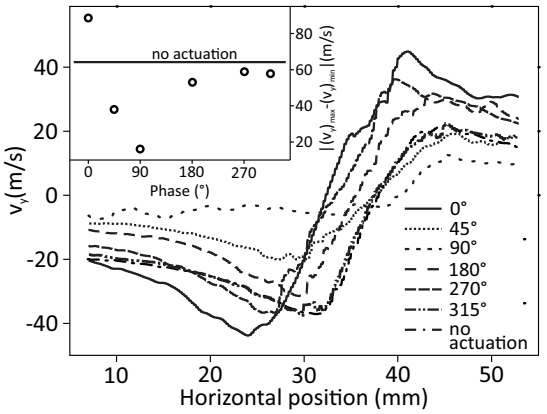

Figure 24: Tangential velocity component along horizontal cut sections through the vortex for different control phases of a $3/rev$ control and a vortex age of $\psi_v = 11.2°$, blade 3, $U_3 = 600V$

The horizontal and vertical shift in vortex position is plotted in Fig. 25 resulting in a vortex trajectory. With the flap amplitude responding harmonically, the tip vortex is released at

different vertical positions for each control phase. The vortex position right behind the blade is plotted at the right side of Fig. 25 and should correlate with the harmonic changes in the vertical blade tip position.

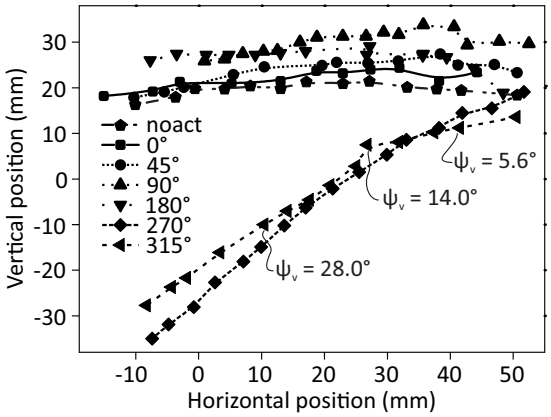

Figure 25: Trajectories of the blade tip vortices for different control phases of a $3/rev$ control, blade 3, $U_3 = 600V$

However, LED and SPR measurements showed rather high variations in flap deflection of about $15\ mm$ during the tests while the $3/rev$ flap tip amplitude was identified at about $5\ mm$ (please note that LED and SPR analysis are based on an averaging of the images taken, thus eliminating fluctuations from the blade motion results). Therefore, it is not possible to evaluate if the variation in vortex position right behind the trailing edge results from the vertical blade tip position due to the active control or due to fluctuations in the flow.

Yet, a clear trend can be observed for control phases of $270°$ and $315°$, where a clear downward convection of the tip vortex over time becomes visible. Due to the alteration in blade lift resulting from the harmonic blade response in torsion, also the downwash experiences a harmonic change. As described above, the maximum elastic torsion response and according to that the maximum change in angle of attack occurs for a control phase between $270°$ and $315°$. Thus, the downwash would also become maximal causing an increased vertical deflection of the tip vortices compared to the passive rotor. In contrast, the trajectories for other control phases show only little deviation from the case without actuation. Here, the vortex position is convected almost horizontally inward from the blade tip.

4. Conclusions

DLR's active twist model rotor has been tested at the rotor preparation hall of DLR Braunschweig. The tests were carried out to set-up the model rotor as well as the test rig and to proof their full functionality for a DNW wind tunnel entry that was planned in the framework of the STAR consortium. Due to irreparable damages in the piezoceramics of the MFC actuators, this set of blades did not proceed towards the wind tunnel.

Despite of the actuator issue, a comprehensive data base has been gained for different applications of active twist in hover during the test campaign and the most important results are summarized in the following:

- The MFC actuators were used for excitation of the rotating blade and the natural blade frequencies for flap bending and torsion were determined.
- Static active twist could be achieved as expected in the order of magnitude of $0.25°/100\ V$ but the improvement in FM due to static active twist was found to lie within the measurement accuracy for 40% of the maximum voltage.
- Although the active twist amplitudes for harmonic control were limited to only 60% of the full control authority, meaningful elastic tip twist could be achieved for a 2, 3, and $4/rev$ control frequency. Accordingly, the active twist excitation showed high influence on the blade motion and its radial deformation.
- A distinct change of the vortex trajectories was observed for a $3/rev$ control with a severely increased initial vertical convection rate. Furthermore, a notable change in the magnitudes of the velocity field around the tip vortex was found. The PIV results showed that the active twist actuation had a high control authority over the strength of the blade tip vortices.
- A new control principle in terms of TPP was applied for a 0, 1, and $2/rev$ control to the active twist model rotor and its feasibility could be demonstrated.

Concluding it can be stated that the functionality of the active twist concept could be proved for different applications in hover. The control authority of the active twist could be demonstrated for basic rotor data as rotor thrust and performance, but also for blade deformation and tip vortex measurements.

Acknowledgments

The long-term support of the STAR partners from the beginning of the project in 2009 until today is highly appreciated. Their technical and financial support into the test at DLR Braunschweig were very valuable and supported significantly to the progress of the program and the preparation of the tests.

REFERENCES

[1] Kessler, C., *Active Rotor Control for Helicopters, Motivation and Survey on Higher Harmonic Control*,$36th$ European Rotorcraft Forum, Paris, France, 2010

[2] Kessler, C., *Active Rotor Control for Helicopters, Individual Blade Control and Swashplateless Rotor Designs*, $36th$ European Rotorcraft Forum, Paris, France, 2010

[3] Straub, F. K., Byrns, E. V., Jr., *Application of Higher Harmonic Blade Feathering on the OH-6A Helicopter for Vibration Reduction*, NASA Contractor Report 4031, 1986

[4] Miao, W., Kottapalli, S. B. R., Frye, M. M., *Flight Demonstration of Higher Harmonic Control (HHC) on S-76*, $42nd$ Annual Forum of the American Helicopter Society, Washington, D. C., USA, 1986

[5] Polychroniadis, M., Achache, M., *Higher Harmonic Control, Flight Tests of an Experimental System on SA 349 Research Gazelle*, $42nd$ Annual Forum of the American Helicopter Society, Washington, D. C., USA, 1986

[6] Splettstoesser, W. R., Kube, R., Seelhorst, U., Wagner, W., Boutier, A., Micheli, F., *Higher Harmonic Control Aeroacoustic Rotor Test (HART) - Test Documentation and Representative Results* -, DLR IB 129-95/28, Braunschweig, Germany, 1995

[7] van der Wall, B. G., *2nd HHC Aeroacoustic Rotor Test (HART II) - Part I, Test Documentation* -, DLR IB 111 - 2003/31, Braunschweig, Germany, 2003

[8] van der Wall, B. G., Burley, C. L., *2nd HHC Aeroacoustic Rotor Test (HART II) - Part II, Representative Results* -, DLR IB 111 - 2005/03, Braunschweig, Germany, 2005

[9] Roth, D., *Advanced Vibration Reduction by IBC Technology*, $30th$ European Rotorcraft Forum, Marseilles, France, 2004

[10] Roth, D., Enenkl, B., Dieterich, O., *Active Rotor Control by Flaps for Vibration Reduction - Full Scale Demonstrator and First Flight Test Results* -, $32nd$ European Rotorcraft Forum, Maastricht, The Netherlands, 2006

[11] Straub, F. K., Anand, V. R., Birchette, T. S., Lau, B. H., *Wind Tunnel Test of the SMART Active Flap Rotor*, $65th$ Annual Forum of the American Helicopter Society, Grapevine, TX, USA, 2009

[12] Cesnik, C. E. S., Shin, S., Wilkie, W. K., Wilbur, M. L., Mirick, P. H., *Modeling, Design, and Testing of the NASA/ARMY/MIT Active Twist Rotor Prototype Blade*, $55th$ Annual Forum of the American Helicopter Society, Montreal, Canada, 1999

[13] Wilbur, M. L., Yeager, W. T., JR., Wilkie, K. W., Cesnik, C. E. S., Shin, S., *Hover Testing of the NASA/ARMY/MIT Active Twist Prototype Blade*, $56th$ Annual Forum of the American Helicopter Society, Virginia Beach, VA, USA, 2000

[14] Wilbur, M. L., Mirick, P. H., William T. Y., JR., Langston, C. W., Cesnik, C. E. S., Shin, S., *Vibratory Loads Reduction Testing of the NASA/ARMY/MIT Active Twist Rotor*, $57th$ Annual Forum of the American Helicopter Society, Washington, DC, USA, 2001

[15] Wilbur, M. L., William, T. Y., JR., Sekula, M. K., *Further Examination of the Vibratory Loads Reduction results from the NASA/ARMY/MIT Active Twist Rotor Test*, $58th$ Annual Forum of the American Helicopter Society, Montreal, Canada, 2002

[16] Booth, E. R., Jr., Wilbur, M. L., *Acoustic Aspects of Active-Twist Rotor Control*, $58th$ Annual Forum of the American Helicopter Society, Montreal, Canada, 2002

[17] Riemenschneider, J., Wierach, P., Opitz, S., Hoffmann, F., *Testing and Simulation of an Active Twist Rotor Blade*, Adaptronic Congress, Göttingen, Germany, 2007

[18] Wierach P., Riemenschneider J., Opitz S., Hoffmann F., *Experimental Investigation of an Active Twist Model Rotor Blade under Centrifugal Loads*, $33rd$ European Rotorcraft Forum, Kazan, Russia, 2007

[19] Hoffmann, F., Opitz, S., Riemenschneider, J., *Validation of Active Twist Modeling Based on Whirl Tower Tests*, $65th$ Annual Forum of the American Helicopter Society, Grapevine, TX, USA, 2009

[20] Riemenschneider, J., Keimer, R., Kalow, S., *Experimental Bench Testing of an Active-Twist Rotor*, $39th$ European Rotorcraft Forum, Moscow, Russia, 2013

[21] Gelhaar, B., Junker, B., Wagner, W., *DLR Rotor Teststand Measures Unsteady Rotor Aerodynamic Data*, $19th$ European Rotorcraft Forum, Cernobbio (Como), Italy, 1993

[22] Mueller, R. H. G., Pengel, K., van der Wall, B. G., *Stereo Pattern Recognition - the Technique for Reliable Rotor Blade Deformation and Twist Measurement*, Paper No. T121 - 3, Heli Japan 2002, AHS International Meeting on Advanced Rotorcraft Technology and Life Saving Activities, Tochigi, Utsunomiya, Japan, 2002

[23] Schneider, O., *Analysis of SPR measurements from HART II*, Aerospace Science and Technology, vol. 9, no. 5, pp. 409-420, Elsevier, 2005

[24] van der Wall, B. G., *Vortex Characteristics Analysed from HART Data*, $23rd$ European Rotorcraft Forum, Dresden, Germany, 1997

[25] Heineck, J. T., Yamauchi, G. K., Woodcock, A. J., Laurenco, L., *Application of Three-Component PIV to a Hovering Rotor Wake*, $56th$ Annual Forum of the American Helicopter Society, Virginia Beach, VA, USA, 2000

[26] van der Wall, B. G., Richard, H., *Analysis Methodology for 3C-PIV data of Rotary Wing Vortices*, Experiments in Fluids, vol. 40, pp. 798-812, 2006

[27] Raffel, M., Willert, C., Wereley, S., Kompenhans, J., *Particle Image Velocimetry - a practical guide*, Springer, 2007

[28] Johnson, B., Leishman, J. G., Sydney, A., *Investigation of Sediment using High-Speed Particle Image Velocimetry*, Journal of the American Helicopter Society, vol. 55, no. 4, pp. 42003-1-42003-16, 2009

[29] Raffel, M., Richard, H., Meier, G. E. A., *On the Applicability of Background Oriented Optical Tomography for Large Scale Aerodynamic Investigations*, Experiments in Fluids, vol. 28, no. 5, pp. 477-481, 2000

[30] McAlister, K. W., *Rotor Wake Development During the First Revolution*, Journal of the American Helicopter Society, vol. 49, no. 4, pp. 371-390, 2004

[31] Leishman, G. J., *Principles of Helicopter Aerodynamics*, Cambridge University Press, USA, 2000